Insights into the effects of surface/bulk defects on photocatalytic hydrogen evolution over TiO$_2$ with exposed {001} facets

Hao Zhang[a,b], Jinmeng Cai[a,b], Yating Wang[a,b], Moqing Wu[a,b], Ming Meng[a,b], Ye Tian[a,b], Xingang Li[a,b,*], Jing Zhang[c], Lirong Zheng[c], Zheng Jiang[d], Jinlong Gong[a,e,*]

[a] Collaborative Innovation Center for Chemical Science & Engineering (Tianjin), School of Chemical Engineering & Technology, Tianjin University, Tianjin, 300072, PR China
[b] Tianjin Key Laboratory of Applied Catalysis Science & Engineering, Tianjin, 300072, PR China
[c] Beijing Synchrotron Radiation Facility, Institute of High Energy Physics, Chinese Academy of Sciences, Beijing, 100049, PR China
[d] Shanghai Synchrotron Radiation Facility, Shanghai Institute of Applied Physics, Chinese Academy of Sciences, Shanghai, 201800, PR China
[e] Key Laboratory for Green Chemical Technology of Ministry of Education, Tianjin, 300072, PR China

ARTICLE INFO

ABSTRACT

This paper describes the effects of defect distribution on energy band structure and the subsequent photocatalytic activity over TiO$_2$ with exposed {001} facets as the model catalyst. Our results show that only surface oxygen vacancies (V$_o$'s) and Ti^{3+} centers in TiO$_2$ can be induced by hydrogenation treatment, whereas the generation of bulk V$_o$'s and Ti^{3+} species depends on the thermal treatment in nitrogen. Both the surface and bulk defects in TiO$_2$ can promote the separation of electron-hole pairs, enhance the light absorption, and increase the donor density. The presence of surface and bulk defects in TiO$_2$ can not change the valence band maximum, but determine the conduction band minimum. Surface defects in TiO$_2$ induce a tail of conduction band located above the H$^+$/H$_2$ redox potential, which benefits the photocatalytic performance. However, bulk defects in TiO$_2$ generate a band tail below the H$^+$/H$_2$ potential, which inhibits hydrogen production. Thus, the change of band gap structure by defects is the major factor to determine the photocatalytic activity of TiO$_2$ for hydrogen evolution. It is a new insight into the rational design and controllable synthesis of defect-engineered materials for various catalytic processes.

1. Introduction

Photocatalysis is a promising strategy for clean hydrogen production from water [1]. With a suitable band structure, TiO$_2$ is regarded as the benchmark material in photocatalytic reactions, and makes hydrogen evolution reaction thermodynamically possible [2,3]. Thus, enormous strategies have been developed to improve the photoactivity of TiO$_2$ nanomaterials, for example, the energy band engineering [4,5], the surface/interface control [6,7], and the morphology fabrication [8,9]. Chen et al. first reported that defect-engineered TiO$_2$ nanomaterials can be obtained at 200 °C for 5 days in high-pressure hydrogen atmosphere, and the as-prepared black TiO$_2$ showed enhanced photocatalytic activity [10]. The defects lead to the changes of optical property and energy band structure of TiO$_2$ and act as the key role on the enhanced photocatalytic performance [10]. To overcome the disadvantages of the rigorous reaction conditions, for example, the long hydrogenation time, high pressure, and explosion risks resulting from

the utilization of pure H$_2$, we developed a concept of hydrogen spillover enhanced hydrogenation by adding a small amount of Pt to the pristine TiO$_2$ [11]. With the aid of hydrogen spillover on Pt, the TiO$_2$ nanomaterials can be efficiently hydrogenated in 8 vol% H$_2$/N$_2$ at normal pressure. Additionally, a Schottky barrier can be formed at the Pt/TiO$_2$ interface, which facilitates charge separation, resulting in the enhanced photoactivity [12].

Generally, defects are deemed as the recombination and trapping centers between photo-generated charge carriers, leading to a decrease in the photocatalytic activity [1]. However, other researchers thought that the induced defects in TiO$_2$ improved charge carrier separation and transportation, and suppressed the recombination of photogenerated carriers [13,14]. Presently, the function of defect distribution of TiO$_2$ is still under debate in photocatalytic process. Kong et al. found that increasing the relative concentration ratio of surface defects to bulk defects could improve the photocatalytic activity because of the enhanced separation efficiency of photo-generated electrons and holes [15]. Yan

---

et al. elucidated that surface oxygen vacancy clusters in TiO_2 could promote the separation of charge carriers and increase the activity during photocatalytic reaction [16]. Furthermore, Leshuk et al. demonstrated that the hydrogenated TiO_2 exhibited the worse photocatalytic activity compared with the pristine TiO_2, and attributed it to the formation of bulk defects after hydrogenation [17]. However, it is reported that the disordered TiO_2 with a high concentration of bulk defects showed the better photocatalytic activity than the surface defect dominant TiO_2 [18]. Pei et al. reported that the bulk defect-engineered TiO_{2-x} showed an enhanced H_2 production rate, and the authors elucidated that bulk trapping could suppress the recombination of charge carriers [19]. Based on the above analysis, the role of defects in TiO_2 for photocatalytic reactions is still unclear. In this sense, a bridge between defect engineering and the tunable properties of TiO_2-based nanomaterials must be established.

Yang et al. first synthesized anatase TiO_2 single crystals with a large percentage (47%) of the high energy {001} facets [20]. Previous studies elucidated that the catalytic performance of TiO_2 {001} facets is higher than that of the thermodynamically stable {101} facets. The higher surface energy of TiO_2 {001} facets can benefit the dissociative adsorption of reactant molecules compared with {101} facets due to the high density of unsaturated coordination Ti atoms, low coordination numbers of exposed atoms and active oxygen atoms with wide bond angles of Ti-O-Ti in {001} facets [7]. Subsequently, the {001}-faceted TiO_2 nanomaterials have attracted a broad interest for their superior physicochemical properties [7,21,22]. Wang et al. demonstrated that the enhanced photocatalytic activity of the hydrogenated TiO_2 with exposed {001} facets for methylene blue (MB) decomposition resulted from the induced Ti^{3+} species and oxygen vacancies [23]. Yu et al. elucidated that the distribution of the Ti^{3+} irons and V_o's was critical in enhancing the photoactivity of MB degradation [24]. Liu et al. reported that the Ti^{3+}/V_o's sites and the coexposed {101} and {001} facets of the TiO_2 nanocrystals could promote CO_2 photoreduction activity [6]. Previous discussion about defect-engineered TiO_2 with exposed {001} facets mainly focused on MB degradation and CO_2 reduction. Recently, Chen et al. reported that the hydrogenated {001}-facet-dominant TiO_2 nanocrystals were more active in photocatalytic hydrogen evolution than the hydrogenated TiO_2 nanocrystals with {101} and {100} facets [25]. The enhanced activity could be ascribed to the electric field generated between stoichiometric surface and reduced subsurface [25].

In spite of the promising photocatalytic features of defect-engineered TiO_2 with exposed {001} facets, little attention has been paid concerning the explanation of the relationship between defect distribution (surface or bulk) and photocatalytic activity of H_2 production. Additionally, the hydrogenation treatment is usually conducted at high temperatures [18,26]. No attempt has been made to elucidate the defect formation mechanism during the simultaneous thermal treatment and hydrogenation. In this work, we chose the TiO_2 single crystal with exposed high energy {001} facets as the model catalyst, and the concept of hydrogen spillover enhanced hydrogenation on Pt was utilized for defect fabrication. We revealed the formation mechanism for the surface and bulk defects in TiO_2 during the thermal hydrogenation process and distinguished the effects of the surface and bulk defects on energy band structure of TiO_2 for photocatalytic hydrogen evolution from water. This work may provide a deep insight into the rational design and fabrication of defect-engineered nanomaterials for various photocatalytic processes.

2. Experimental section

2.1. Materials synthesis

Pristine TiO_2 with exposed {001} facets were synthesized by a solvothermal method. In a typical procedure, 25 g of tetrabutyl titanate (TBT) was mixed with 3.5 mL of 40 wt% HF solution, under stirring for 20 min in a 100 mL Teflon-lined autoclave. Thereafter, the autoclave

was kept at 180 °C for 24 h. After solvothermal reaction, the sample was cooled down to room temperature. The resulting white precipitates were collected and washed with absolute ethanol and distilled water for several times, and then the sample was dried at 80 °C for 6 h in vacuum, and the corresponding sample was donated as TP. The sample of TP with 1 wt% Pt loaded was synthesized by using the conventional wetness impregnation method. Typically, 1 g of the sample of TP was immersed into a certain amount of $H_2PtCl_6·6H_2O$ aqueous solution to acquire a slurry, which was subsequently dried at room temperature overnight, and then the dried powder was dispersed into 200 mL deionized water and reduced by 280 mg of $NaBH_4$. By centrifugation, the sample was obtained and washed with deionized water for several times, and later dried at 80 °C overnight. With the aid of Pt, the hydrogen spillover enhanced hydrogenation treatment of the samples was conducted. Briefly, the sample of TP with 1 wt% Pt was treated in a quartz tube furnace at 500, 700, and 850 °C for 5 h with the flow rate of 50 mL/min in 8 vol% H_2/N_2 flow and the corresponding samples were donated as TH500, TH700, and TH850, respectively. The removal of surface fluorine ions and formation of surface disorder can be accomplished during this process. Moreover, the sample of TP loaded with 1 wt% Pt was annealed at 700 °C in pure nitrogen atmosphere (50 mL/min) for 5 h, and the achieved sample was donated as TN700. For comparison, the sample of TP was pre-treated in an oven at 550 °C for 2 h to remove the surface fluorine ions and then loaded with 1 wt% Pt using the above method, and the corresponding sample was donated as TC. In addition, the sample of TP was washed using 1 M NaOH solution to remove the surface fluorine and then loaded with 1 wt% Pt, and the corresponding sample was donated as TW. The sample of TW was treated at 700 °C for 5 h in 8 vol% H_2/N_2 flow and the corresponding sample was donated as TW-H700.

2.2. Material characterizations

The X-ray diffraction (XRD) patterns of the samples were recorded on a D8 Focus (Bruker) diffraction instrument operating at 200 mA and 40 kV, using Cu Kα as the radiation source (λ = 0.15418 nm), and the sizes of nanocrystals were calculated using Scherrer equation based on XRD results. The images of transmission electron microscopy (TEM), high resolution transmission electron microscopy (HRTEM), high angle annular dark field scanning transmission electron microscopy (HAADF-STEM), bright field scanning transmission electron microscopy (BF-STEM), as well as the corresponding STEM-EDS element analysis and selected area electron diffraction pattern (SAED) were obtained using a JEOL JEM-2100F field emission electron microscope operating at 200 kV with an EDAX energy disperse spectroscopy. Electron energy loss spectra (EELS) and the corresponding HAADF-STEM images were recorded on a FEI Tecnai G^2 F20 microscope equipped with field emission gun and Gatan GIF Tridiem 863 energy filter. The scanning electron microscopy (SEM) images of the samples were taken on a Hitachi S-4800 scanning electron microscope. Visible Raman spectra were obtained on NT-MDT NTEGRA Spectra system using a laser wavelength of 473 nm. Ultraviolet (UV) Raman spectra were performed on Renishaw inVia reflex system using a laser wavelength of 325 nm. X-ray photoelectron spectroscopy (XPS) was conducted on a PHI-1600 ESCA spectrometer using Mg Kα (1253.6 eV) as radiation source. Before analysis, the samples were placed in vacuum at 80 °C overnight to remove the adsorbed substances. The UV–vis diffuse reflectance spectra (UV-vis DRS) of the samples were recorded on a Perkin-Elmer Lambda 750S UV-vis-NIR spectrometer equipped with an integrating sphere. The UV–vis DRS results were recorded from the wavelength of 200–800 nm against barium sulfate. X-ray absorption fine structure (XAFS) measurements were performed at 1W1 B beamline of Beijing Synchrotron Radiation Facility (BSRF) and BL14W1 beamline of Shanghai Synchrotron Radiation Facility (SSRF). The Ti K-edge absorption spectra were recorded in transmission mode. The photoluminescence measurement (PL) was performed on the Horiba Jobin

Yvon Fluorolog3 photoluminescence spectrometer at room temperature using the excitation wavelength of 325 nm. The electron paramagnetic resonance (EPR) spectra were recorded with a Bruker A300 spectrometer at room temperature operated at X band frequency (9.77 GHz) and 100 kHz field modulation. The specific surface area (S_{BET}) measurement was carried out on Quantachrome QuadraSorb SI at −196 °C. Before the analysis, the samples were degassed at 300 °C for 3 h to remove the adsorbed surface species. The S_{BET} was determined from the linear part of the BET curve.

2.3. Photocatalytic activity measurement

The hydrogen evolution experiments were carried out in the Labsolar-III AG system (Perfectlight), as shown in Fig. S1. In a typical procedure, 25 mg of the powdered sample was dispersed by sonicating in 100 mL of methanol aqueous solution (1:1 by volume). Methanol is the sacrificial agent of the reaction and serves as an electron donor. The temperature of the aqueous solution was maintained at 7 °C using cooling water during the reaction. The light source was a 300 W Xe lamp equipped with an AM 1.5G filter. The luminous power measured at the central point of reactant is ∼ 700 mW cm^{-2} using a PM100D power meter (Thorlabs). The generated H_2 was measured per 0.5 h by a gas chromatography (Fuli Instrument) according to a standard curve. The apparent quantum efficiencies of the powdered samples were determined using a 300 W Xe lamp (Aulight) equipped with a 365 nm bandpass filter. 70 mg of the sample was dispersed in 100 mL of methanol aqueous solution (1:1 by volume). The irradiation intensity measured using a PM100D power meter is 83 mW cm^{-2}, and the irradiation area is 36.3 cm^2. The AQE of the samples was calculated using equation (1).

$$AQE = \frac{2MN_A hc}{AIt\lambda} \times 100\% \tag{1}$$

where M is the amount of hydrogen molecules, N_A is the Avogadro's constant, h is Planck constant, c is the light velocity, I is the intensity of the light, A is the irradiation area, t is the reaction time, and λ is the wavelength of light.

The photoreduction of Cr^{6+} to Cr^{3+} were tested under simulated solar light irradiation using a 300 W Xe lamp equipped with an AM 1.5G filter. The luminous power tested at the center of reactant was ∼ 153 mW cm^{-2} using a PM100D power meter (Thorlabs). In a typical procedure, 30 mg of photocatalyst was suspended in 50 mL Cr^{6+} solution (100 mg L^{-1}) containing 10 mL methanol. Methanol serves as the sacrificial agent of the photoreduction reaction. The temperature of the suspension was maintained at 7 °C using cooling water during the reaction. The suspension was stirred in dark for 30 min to establish adsorption-desorption equilibrium. During the reaction, 2 mL of the suspension was taken at specific time intervals and been centrifuged to remove the photocatalyst. The concentration of Cr^{6+} was tested using 1,5-diphenylcarbazide (DPC) method by measuring the absorption at 540 nm using a UV–vis spectrometer (Perkin-Elmer Lambda 750S).

2.4. Photoelectrochemical analysis

Photoelectrochemical analysis was performed on CHI 660E electrochemistry workstation (Chenhua Instrument). Chronoamperometry tests were conducted at 0.5 V in a standard three electrode system with Pt foil as counter electrode and Ag/AgCl electrode as the reference electrode. For a typical procedure to make working electrodes on FTO glass, 2 mg of powder and 20 μL of Nafion solution were dispersed in 0.1 mL absolute ethanol and 0.4 mL distilled water to form a homogeneous ink, and 20 μL ink was loaded onto a 1 cm^2 FTO glass via drop-coating technique. An AM 1.5G solar power system (Perfectlight) was used as the irradiation source. Electrochemical impedance spectra (EIS) were conducted in the frequency range of 1 Hz to 100 kHz, and Mott-

Table 1
H_2 production rates and apparent quantum efficiencies of the as-prepared samples.

Samples	H_2 production rate		AQE (%)
	$r_M{}^a$ (μmol g^{-1} h^{-1})	$r_S{}^b$ (μmol m^{-2} h^{-1})	
TC	4089.6	118.5	17.5
TW	8832.6	65.9	55.7
TH500	7740.4	230.4	39.7
TH700	15130.8	617.6	70.3
TH850	923.1	177.5	15.0
TN700	2387.7	144.7	16.0

^a Rates normalized to mass of the as-prepared samples.
^b Rates normalized to specific surface area of the as-prepared samples.

[a] Rates normalized to mass of the as-prepared samples.
[b] Rates normalized to specific surface area of the as-prepared samples.

Schottly plots were performed using glassy carbon electrodes at the frequency of 1 kHz.

3. Results and discussion

Fig. S2 shows the profiles of photocatalytic hydrogen production, the constant and stable amounts of H_2 were produced over all of the as-prepared samples under simulated solar light irradiation. The hydrogen evolution rates and the apparent quantum efficiencies were summarized in Table 1. The sample of TH700 shows a photocatalytic hydrogen evolution rate of 15130.8 μmol g^{-1} h^{-1}, which is 1.7-fold and 3.7-fold than the samples of TW and TC, respectively. Additionally, the specific surface areas of the as-prepared samples sharply decrease after hydrogenation or thermal treatment in nitrogen, as listed in Table S1. To better understand the photocatalytic performance, rates normalized to specific surface area were calculated, and the sample of TH700 is 9.4 and 5.2 times higher than the samples of TW and TC. Here, we show that 700 °C is the optimal hydrogenation temperature of TiO$_2$ to reach the best performance for photocatalytic hydrogen evolution, and the apparent quantum efficiency of the sample of TH700 is 1.3–4.7 times higher than other as-prepared samples. When we increase the temperature to 850 °C, the hydrogen evolution rates dramatically decrease compared with the samples of TH500 and TH700. Compared with the sample of TH700, the sample of TN700 shows quite a low hydrogen evolution rate, which suggests that hydrogenation is significant to improve the hydrogen production efficiency.

Fig. 1 shows the XRD patterns of the as-prepared samples. The samples of TW, TC, TH500, TH700, and TN700 exhibit a group of diffraction peaks, which can be attributed to anatase phase (JCPDS No.21-1272). After further increasing the hydrogenation temperature to 850 °C, an obvious peak at 27.5° corresponding to {110} plane diffraction of rutile (JPCDS No. 87–920) appears, indicating the phase transformation from anatase to rutile. Moreover, for the sample of
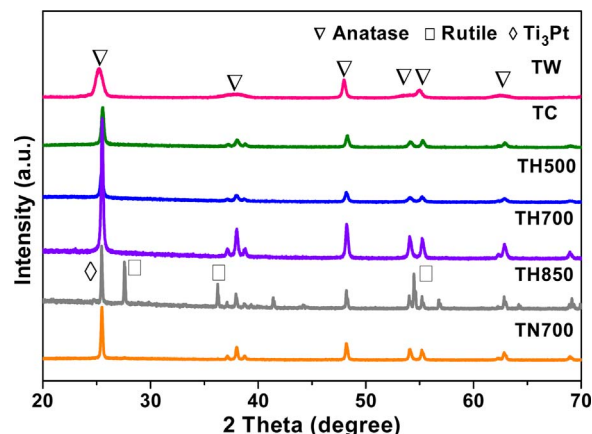

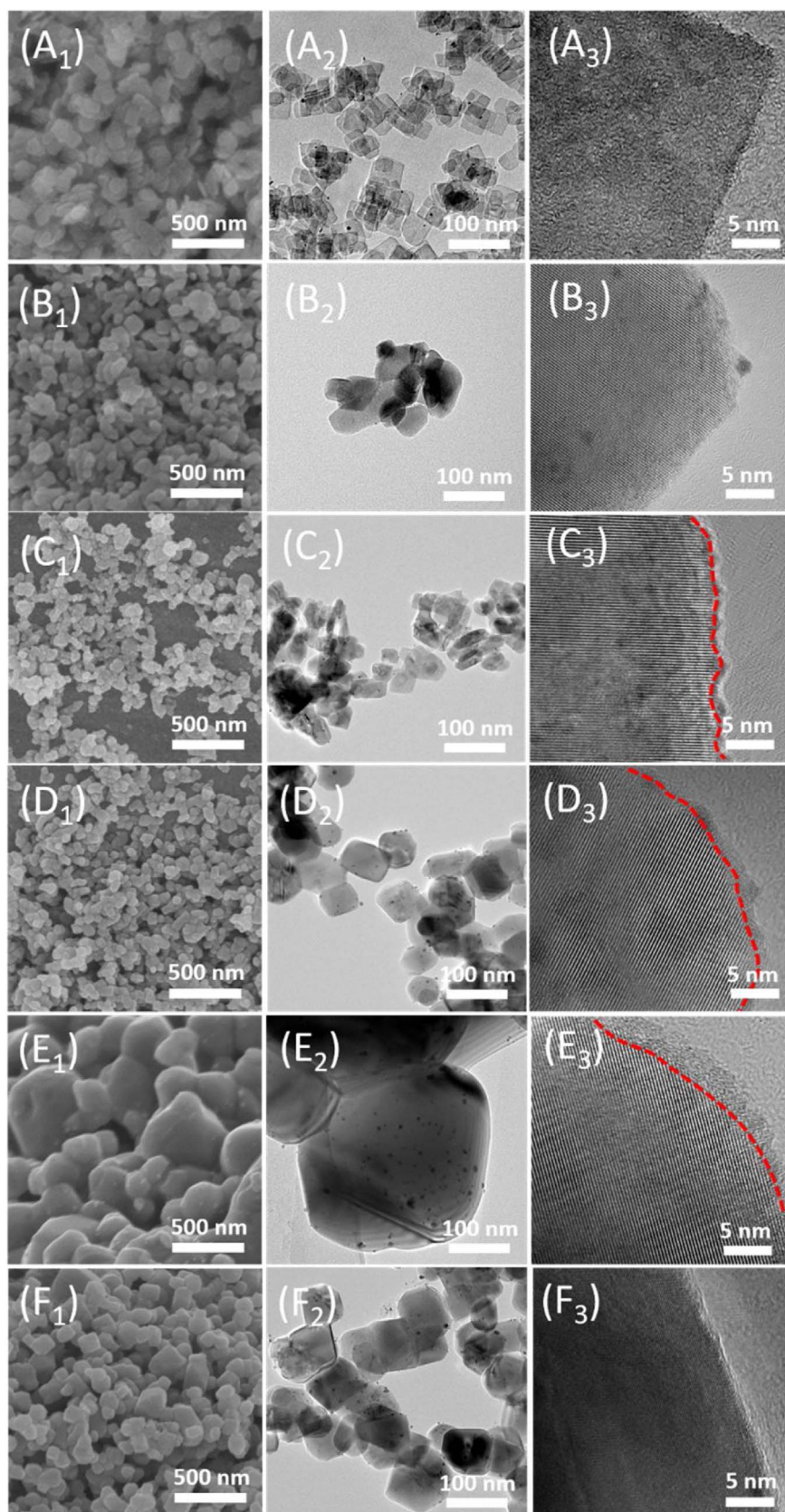**Fig. 1.** XRD patterns of the as-prepared samples.

Fig. 2. SEM images, TEM images and HRTEM images of the as-prepared samples: (A_1, A_2, A_3) TW, (B_1, B_2, B_3) TC, (C_1, C_2, C_3) TH500, (D_1, D_2, D_3) TH700, (E_1, E_2, E_3) TH850, and (F_1, F_2, F_3) TN700.

TH850, a weak peak at 24.8° is observed, which may belongs to the Ti_3Pt phase (JCPDS No. 07-0353). The sample of TH850 shows low hydrogen evolution rate, and it is probably due to the phase transition from anatase to rutile and the formation of the Ti_3Pt alloy [11,27].

Fig. S3 shows the SEM and TEM images of the sample of TP, which consists of the well-defined sheet like morphology with a side length of about 33.1 nm and a thickness of about 4.7 nm (Fig. S3A and S3B). The HRTEM image in Fig. S3C displays the lattice fringe spacing of

0.352 nm and 0.235 nm, which correspond to the (101) facet and (001) facet of anatase TiO_2, respectively. Significantly, the corresponding SAED pattern (inset of Fig. S3A) indicates that the as-prepared sample of TP is well-defined single crystals and the bottom and top facets are {001} facets.

Fig. 2A$_1$-2F$_1$ and 2A$_2$-2F$_2$ show the SEM and TEM images of the as-prepared samples. Compared with the well-defined sheet-shaped sample of TW, the morphology of the samples of TC and TH500 significantly changed. The sheet like TiO_2 single crystals started to fuse together to form nanoparticles. After the hydrogenation treatment at 700 °C for 5 h, the nanocrystals continue to grow. For comparison, the SEM and TEM analysis of the sample of TN700 is also performed, which exhibits a larger crystal size than the sample of TH700, indicating that the hydrogenation treatment could retard the growth of TiO_2 nanocrystals. When we increase the hydrogenation temperature to 850 °C, the nanocrystals continue to grow (Fig. 2E$_1$ and 2E$_2$). In Fig. 2A$_3$-2F$_3$, a disordered surface layer coating on the crystalline core can be clearly observed in the samples of TH500, TH700 and TH850 (labeled by red dash lines in HRTEM images). Nevertheless, the samples of TN700 and TC are complete crystalline, even for the surface layer of the samples. These differences indicate that the surface disorder of the as-prepared samples can only be induced via hydrogenation instead of thermal treatment in pure nitrogen or air [28–30].

Fig. S4 shows the calculated results of average crystalline sizes of the as-prepared samples along [001] and [100] directions according to XRD analysis. The crystalline sizes of the samples of TC and TH500 along the [001] direction significantly increase compared with the sample of TW. Nonetheless, the average crystalline sizes along the [100] direction does not change a lot. It indicates that the growth of TiO_2 nanosheets through hydrogenation treatment mainly occurs along the [001] direction at low temperature via the fusion of {001} facets. With the increase of hydrogenation temperature to 700 °C, the growth along the [100] direction is clearly observed, besides the growth along the [001] direction. For the sample of TN700, the tremendous growth can be both observed along [001] and [100] directions compared with the sample of TH700, which is consistent with the SEM and TEM analysis in Fig. 2.

Fig. 3A shows the HAADF-STEM image of the sample of TH700. No fluorine and other impurities are detected from the profiles of STEM-EDS point scan and STEM-EDS mapping (Fig. 3A-3D), which are supported by the results of the XPS survey spectrum (Fig. S5A) and the F 1 s XPS spectrum (Fig. S5B), as well. It indicates that the surface fluorine has been completely removed through hydrogenation and no impurity is induced during the treatments. To further study the disordered surface layer of TH700, the Fast Fourier Transform (FFT) on the selected

area marked with orange dash line box was performed in Fig. 3E. The two bright spots in Fig. 3F (pointed by red arrows) are selected to perform the Inverse Fast Fourier Transform (IFFT), which is shown in Fig. 3G. The IFFT image shows significantly disordered area of destroyed lattice, suggesting the disordered nature of the surface layer on the sample of TH700. Fig. S6 shows the HAADF-STEM images (Fig. S6A) and BF-STEM images (Fig. S6B) collected from the same area of the sample of TH700. The Pt nanoparticles are uniformly dispersed on TiO_2 nanosheets, which can benefit the hydrogenation process through hydrogen spillover on Pt. The amorphous surface layer is often observed in defect-engineered TiO_2 nanomaterials, for example, the hydrogenated TiO_2 [10,29], Al-reduced titania nanocrystals [31,32], and H_2 plasma treated TiO_2 [33]. The amorphous layer may consist of defects including Ti^{3+} species and V_o's, and it can also induce the color change [26].

Raman spectra are often utilized to characterize the structure of samples. In Fig. S7, the Raman shifts locating at ∼ 144 cm^{-1}, ∼ 391 cm^{-1}, ∼ 514 cm^{-1} and ∼ 635 cm^{-1} are attributed to the anatase phase, and the shifts locating at ∼ 237 cm^{-1}, ∼ 440 cm^{-1} and ∼ 600 cm^{-1} are assigned to the rutile phase. For TiO_2 nanomaterials with exposed {001} facets, only the unsaturated 5c-Ti and 2c-O bonding modes are distributed on the surface, which makes the number of symmetric stretching vibration modes of O-Ti-O become less. The E_g peak is mainly caused by symmetric stretching vibration of O-Ti-O, and the A_{1g} peak is caused by antisymmetric bending vibration of O-Ti-O in TiO_2. Since the vibrational modes E_g and A_{1g} peaks can be related to different crystal planes, the percentage of the exposed TiO_2 {001} facets could be calculated through ratio of intensity of the A_{1g} and E_g peaks via Raman analysis (Table S2) [34]. It is worth noticing that the regular morphology has changed after hydrogenation and thermal treatment in nitrogen. Thus, the methods used for the calculation of percentage of exposed {001} facets based on Wulff construction can not be used, such as calculation methods based on SEM, TEM and XRD. The percentage of {001} facets of the sample of TW is 66.7%. As for the samples of TC and TH500, the percentages of {001} facets decrease to 14.3% and 14.4%, respectively. However, when the hydrogenation temperature increases to 700 °C, the percentage of {001} facets starts to increase to 22.8%, which may result from the evident crystal growth through [100] direction. For the sample of TN700, the percentage of {001} facets is 9.5%, and it is much lower than that for the sample of TH700, which attributes to the obvious crystal growth during thermal treatment in nitrogen as shown in XRD and TEM analysis in Fig. S4 and Fig. 2, respectively.

Fig. 4A shows the UV–vis DRS results of the samples. The hydrogenated samples of TH500 and TH700 exhibit the higher light
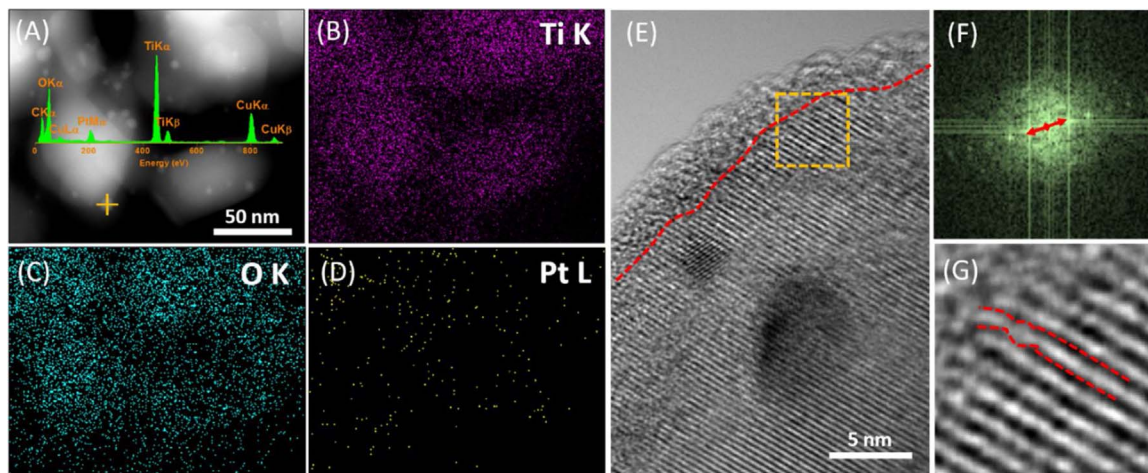

Fig. 3. (A) HAADF-STEM image of the sample of TH700, inset shows STEM-EDS point scan of the orange cross mark, (B, C and D) STEM-EDS-mapping of (A), (E) HRTEM image of the sample of TH700, (F) FFT image of the selected area in (E) marked with a box, and (G) IFFT image performed on the red arrow pointed spots in (F).
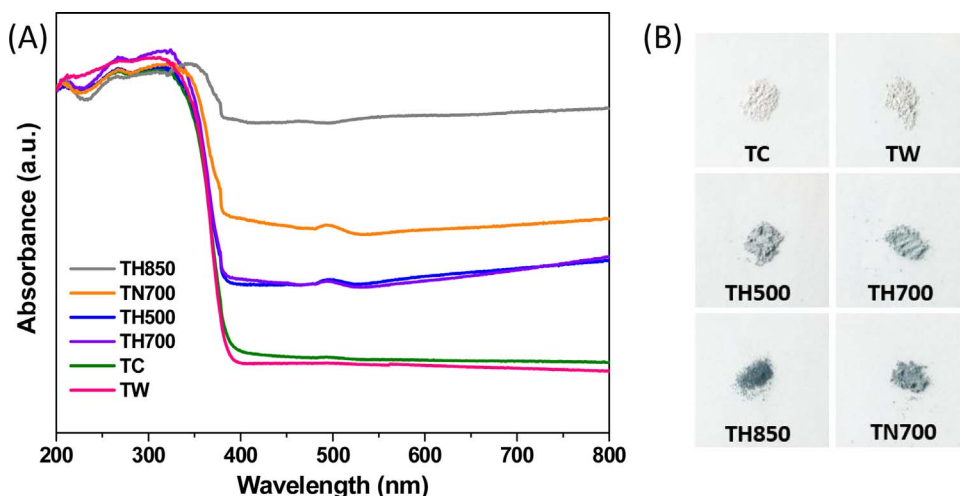
Fig. 4. (A) The UV–vis spectra, and (B) digital photos of the as-prepared samples.

absorption, as compared with the samples of TW and TC. The light absorption of the sample of TN700 is higher than that of the samples of TH500 and TH700. Among these samples, the sample of TH850 shows the highest light absorption, which attributes to the hydrogenation and phase transformation at high temperature. Fig. 4B shows the color of the as-prepared samples. After hydrogenation, the color of the samples of TH500 and TH700 turns to be grey compared with the samples of TW and TC. To further increase the hydrogenation temperature, the color of the sample of TH850 turns to be darker. In addition, the color of the sample of TN700 which treated in pure nitrogen is darker than that for the sample of TH700. Electronic transition in semiconductor from both valence band and defect states to conduction band, as well as from valence band to defect states, is responsible for the light absorption and the subsequent color changes [25,35]. In addition, it is well known that hydrogenation induced Ti^{3+} centers and oxygen vacancies could enhance the light absorption and turn white TiO_2 to black, yellow or blue [18,26]. The changes of absorption and color may reflect the defective nature of the as-prepared samples.

Fig. 5 shows the PL emission spectra of the as-prepared samples to evaluate the charge separation efficiency, since the PL emission attributes from the recombination of free carriers in semiconductor [29]. The samples of TW, TC and TH850 display a strong emission peak in the wavelength range of 350–600 nm. After thermal treatments in hydrogen or nitrogen atmosphere, the peak intensity becomes lower, indicating that both the hydrogenation and thermal treatment in nitrogen could increase the charge separation efficiency. The photoluminescence

emission intensity of the samples of TH500 and TH700 is lower than that of TN700. The sample of TH700 with the highest photocatalytic performance has the lowest emission intensity, which results from the inhibited recombination of photo-generated charge carriers after hydrogenation. In defect-engineered TiO_2, the localization of mid-gap states caused by oxygen vacancies and Ti^{3+} species allows them to act as trapping sites for photo-generated free charge carriers and hinders the recombination of electrons and holes [18,26]. In other words, the decreased emission intensities indicate the presence of defects in the as-prepared samples.

EPR is a sensitive method that allows the detection of paramagnetic species with unpaired electrons either in the surface or bulk regions [18]. Pure TiO_2 exhibits no signal for EPR analysis. However, Ti^{3+} centers and oxygen vacancies in defect-engineered TiO_2 can produce active response. Fig. 6 shows the EPR spectra of the as-prepared samples. The samples of TH700 and TH500 exhibit a strong EPR signal at $g = 2.002$, which is attributed to the oxygen vacancy combined with one electron (V_o's) [36]. The EPR signal of the sample of TH700 is stronger than that of the sample of TH500, indicating the higher concentration of V_o's in the sample of TH700. In addition, the sample of TN700 displays a intensive EPR signal of V_o's, as well as a broad absorption peak at $g = 1.94$-1.99, which can be assigned to a paramagnetic Ti^{3+} center that originates from the short relaxation time of the Ti^{3+} species [24,37,38]. Surface Ti^{3+} species could induce the EPR signals at $g = 2.02$ or at $g = 2.01$ [18,24]. Thus, the strong signal at $g = 1.94 - 1.99$ of the sample of TN700 can be attributed to Ti^{3+} centers located in bulk region. However, no signal can be observed in
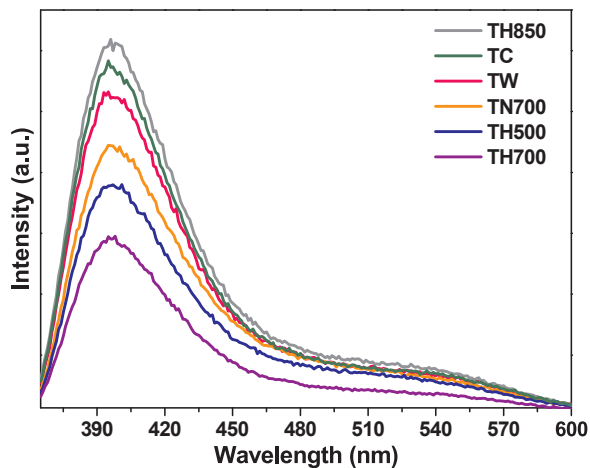

Fig. 5. Photoluminescence emission spectra of the as-prepared samples using the excitation wavelength of 325 nm.
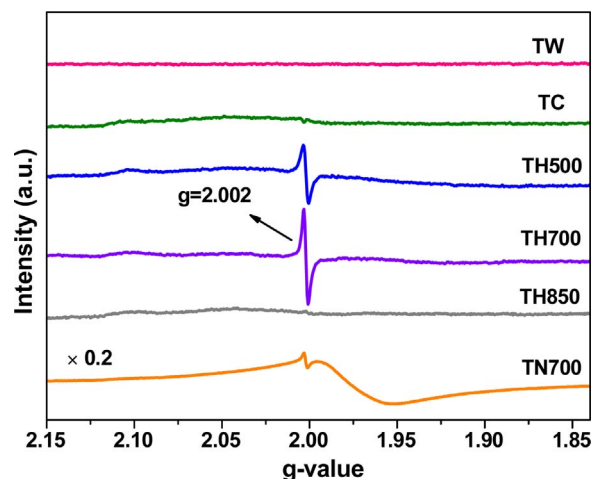

Fig. 6. EPR spectra of the as-prepared samples.

Table 2

Local structural parameters in the first Ti-O shell of Ti *K*-edge EXAFS of the as-prepared samples.

Sample	Shell	C^a	R^b (Å)	σ^{2c} (Å^2)	$\Delta E_0{}^d$ (eV)	R-factor^e (%)
Anatase	Ti-O	6.0	1.939	0.0032	0.636	2.879
TC	Ti-O	6.0	1.939	0.0032	0.876	2.163
TH500	Ti-O	5.7	1.951	0.0033	3.136	1.443
TH700	Ti-O	5.8	1.953	0.0036	2.387	1.857
TN700	Ti-O	5.9	1.954	0.0039	3.251	2.354

[a] Coordination number.
[b] Coordination distance.
[c] Debye-Waller factor.
[d] Inner potential correction.
[e] Residual factor.

this range for the sample of TH700, indicating no bulk Ti^{3+} species generated through hydrogenation. Although no evident signals can be observed in EPR spectra of the as-prepared samples at g = 2.01 or 2.02, an unconspicuous EPR signal at around 2.01 may overlap with the signal of V_o's at g = 2.002 and make the surface Ti^{3+} signal difficultly be detected. In this sense, other techniques should be applied to investigate surface Ti^{3+} species.

To further study the defects induced via the hydrogenation and thermal treatment in nitrogen, XAFS of Ti *K*-edge is investigated. Fig. S8 shows the radial structure functions (RSFs) of the as-prepared samples. The first coordination shell can be ascribed to the scattering of the Ti-O coordination shell. The fitting of the shell was conducted and the curve fitting results accord well with the experimental data (Fig. S9). Table 2 gives the fitting results of the coordination parameters, which clearly reveal the elongated Ti-O band distance and increased Debye-Waller factor of the samples of TH500, TH700 and TN700, compared with the reference anatase and the sample of TC with similar percentage of {001} facets. Theoretical calculation and experiment analysis also proved that the generation of V_o's could lead to the elongation of Ti-O bond length [29,39,40]. The generation of V_o's in the as-prepared samples after hydrogenation and thermal treatment in nitrogen consists with the above EPR results in Fig. 6. Moreover, the sample of TN700 shows a longer Ti-O band distance and a higher Debye-Waller factor, compared with the sample of TH700. In spite of both contain V_o's, the Debye-Waller factor of the sample of TN700 is higher than that of the sample of TH700. It indicates that more obvious disordered crystal structure exists in the bulk region of the sample of TN700.

Generally, XPS is used to evaluate the change of chemical bonding and element binding energy on surface [30]. The O 1 s peaks can be deconvoluted into two peaks (Fig. S10), which are surface Ti-OH groups (O_{OH}) and Ti-O-Ti surface lattice oxygen species (O_L) [8,41]. The O_{OH} peaks of the hydrogenated sample of TH700 exhibit much enhanced intensity as compared with the samples of TC and TN700, suggesting the increased O_{OH} concentration by hydrogenation, as listed in Table S3. Furthermore, the increased concentration of the surface Ti-OH can also improve the surface hydrophilicity of the hydrogenated samples, which can further promote the photocatalytic performance [42,43]. Fig. 7 shows the Ti 2p XPS results of the samples. The binding energies of Ti $2p_{1/2}$ and Ti $2p_{3/2}$ can be observed at ~ 464.5 eV and ~ 458.6 eV, respectively. Moreover, the hydrogenated sample of TH700 shows a distinct shift to lower binding energy compared with the samples of TC and TN700, suggesting surface Ti^{3+} species is obtained via hydrogenation. However, no obvious change can be detected for the sample of TN700 compared with the sample of TC, indicating no Ti^{3+} center locates on the surface of the sample of TN700. To display the XPS results clearly, the difference spectra of Ti 2p XPS results by subtracting TH700 and TN700 with TC are obtained and shown in Fig. 7. Obviously, two peaks centered at ~ 458.2 and ~ 463.6 eV in the difference spectrum of the sample of TH700 are observed, which is in good agreement with the typical Ti $2p_{3/2}$ and Ti $2p_{1/2}$ peaks of Ti^{3+}
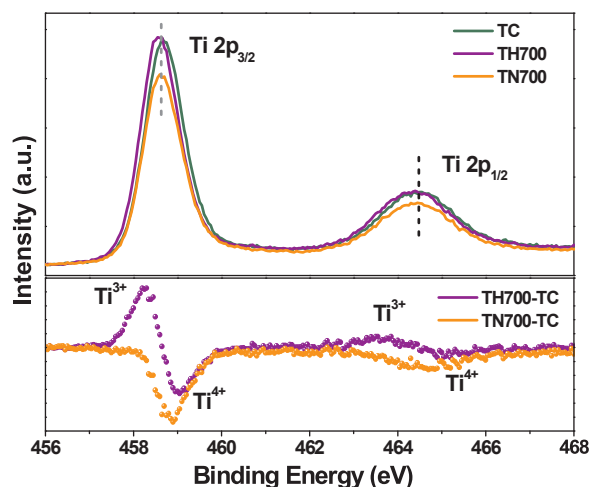

Fig. 7. Ti 2p XPS spectra of TC, TH700, and TN700 as well as the difference spectra of Ti 2p XPS results by subtracting TH700 and TN700 with TC.

[44]. To evaluate the amount of Ti^{3+} in the surface layer of the sample of TH700, the Ti 2p peak is deconvoluted (Fig. S11) and shows a Ti^{3+}/Ti^{4+} atomic ratio of ~ 0.26 in the surface layer.

EELS is a characterization method performed in high vacuum that often used to investigate surface and interface states. Combined with STEM images, we can easily locate the specific positions for analysis. To further confirm the location of Ti^{3+} species, Ti $L_{3,2}$ STEM-EELS spectra of the sample of TH700 collected at surface and bulk regions were performed as shown in Fig. 8A and B, respectively. Since the local octahedral coordination of Ti could be discerned from t_{2g} and e_g peaks, the peak positions were obtained using baseline correction and de-convolution analysis [45]. The corresponding spectral energy positions of peaks are listed in Table S4. In typical Ti oxides, a shift to lower energy by 1.7-2.0 eV of Ti $L_{3,2}$ spectra could be observed per oxidation state [45]. When spectrum is collected at the surface region of the sample of TH700, the peaks shift to lower energies compared with the spectrum collected at bulk region, indicating the reduction of Ti is quite evident on the surface compared with the bulk region. Moreover, the increase of *d* electrons results from the decrease of the formal charge of the Ti (formation of Ti^{3+}), which could increase the occupation number of the antibonding orbital. Thus, the t_{2g}-e_g splitting becomes smaller [46,47]. Comparing the EELS result collected at surface and bulk regions of the sample of TH700, the t_{2g}-e_g splitting is 1.65 eV vs 2.31 eV in L_3 edge and 1.58 eV vs 2.29 eV in L_2 edge. The decrease observed for the peak splitting in the sample of TH700 can also indicate the presence of Ti^{3+} species on its surface region. For comparison, STEM-EELS spectra of the sample of TN700 collected at surface and bulk regions are shown in Fig. 8C and D. No evident difference could be observed between the surface and bulk regions for the sample of TN700. In addition, EELS spectra collected in TEM mode reflect the average information of surface and bulk regions (Fig. S12). And the corresponding spectral energy positions are listed in Table S5. The smaller t_{2g}-e_g splitting can be observed in the samples of TH700 and TN700 compared with the sample of TC, and an obvious shift to lower energy is also observed in the sample of TN700, which may ascribe to the higher content of Ti^{3+} species in the bulk. In consideration of the EELS analysis, Ti^{3+} centers locate in the surface and bulk regions of the samples of TH700 and TN700, respectively, which is in good agreement with the above EPR and XPS results in Fig. 6 and Fig. 7.

Fig. 9 shows the Raman spectra performed using excitation laser wavelength of 325 nm and 473 nm. Small size of the particles (< 10 nm) or shortening of the correlation length results from defects will lead to phonon confinement effects, which cause the blue-shift of the most intense E_g peak [48]. E_g mode is more sensitive to oxygen defects than the Ti-O stretching mode, which makes the change of E_g
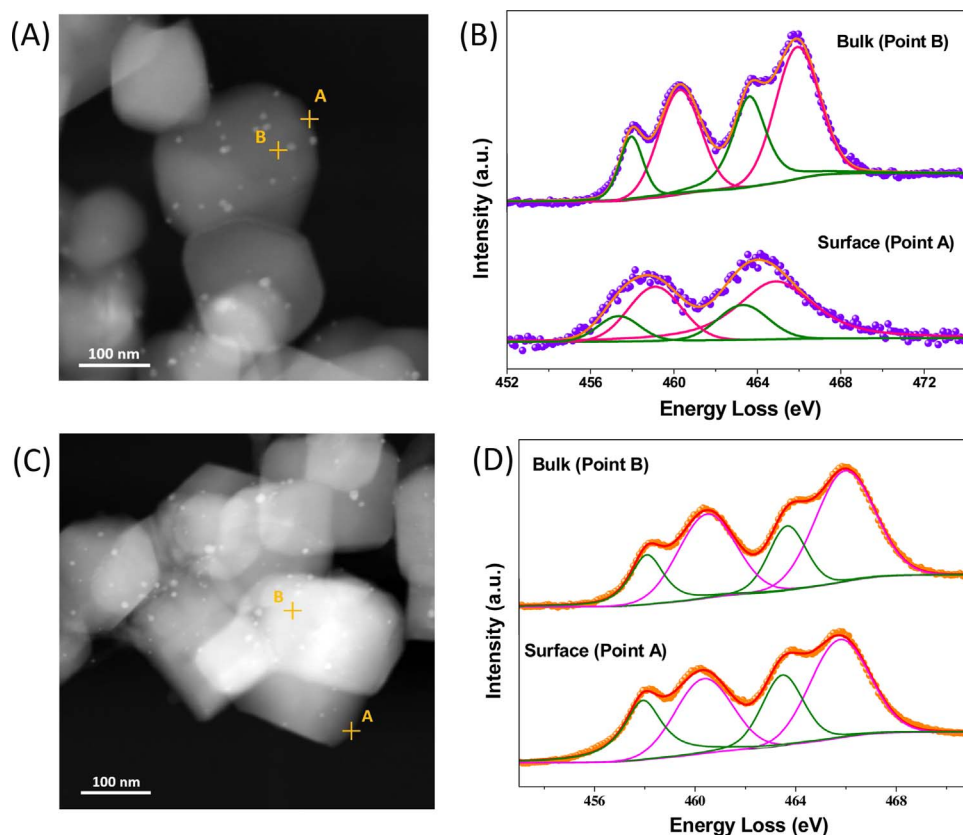
Fig. 8. (A) HAADF-STEM image of the sample of TH700, (B) Ti $L_{3,2}$ STEM-EELS spectra of the sample of TH700 performed at surface (point A) and bulk regions (point B) in (A), (C) HAADF-STEM image of the sample of TN700, (D) Ti $L_{3,2}$ EELS spectra of the sample of TN700 performed at surface (point A) and bulk regions (point B) in (C).

mode serve as the direct evidence of oxygen vacancies [13,17,27]. According to the XRD analysis in Fig. S4, the sizes of crystallites rule out the occurrence of small-size effect, suggesting only oxygen vacancies are responsible for the change of Raman spectra. Raman spectra excited using laser of 473 nm provide the bulk information of the samples (Fig. 9A). Compared with the samples of TC and TH700, the evident blue shift of E_g peak for the sample of TN700 demonstrates the presence of large number of oxygen vacancies in the bulk region. No obvious change can be detected for the sample of TH700 compared with the sample of TC, indicating no bulk V_o's in the sample of TH700. In addition, UV Raman spectroscopy is more sensitive to the surface states of solid samples when the sample absorbs UV light [49–51]. Since TiO_2 strongly absorbs UV light, it is effective to investigate surface states using UV Raman. Clearly, the sample of TH700 exhibits a large blue shift of E_g peak in the Raman spectrum using the laser of 325 nm, indicating the generation of surface oxygen vacancies during hydrogenation (Fig. 9B). However, no evident difference can be observed for the sample of TN700 compared with the sample of TC, which suggests no surface oxygen vacancy locates on the sample of TN700. In addition,

the growth of TiO_2 crystals is through the extension of Ti-O-Ti bridging via dehydration between the hydroxyl groups on the surfaces of the neighbor TiO_2 nanocrystals, and surface oxygen vacancies can retard the extension of the Ti-O-Ti bridging between the neighbor TiO_2 surfaces [52]. Thus, in the XRD results shown in Fig. S4, the restricted growth of the sample of TH700 may results from the presence of a large amount of surface oxygen vacancies induced via hydrogenation treatment. Additionally, the obvious growth of the sample of TN700 indicates that the thermal treatment alone can not induce surface defects to hinder Ti-O-Ti extension.

Based on our present studies, hydrogenation only induces surface Ti^{3+} centers and V_o's, and the thermal treatment in nitrogen only induce Ti^{3+} species and V_o's in the bulk. The depletion of surface and bulk oxygen atoms during hydrogenation and thermal treatment in nitrogen leaves TiO_2 oxygen-deficient. To keep the charge balance, the removing of O atom results in two excess electrons that can be stabilized on neighboring Ti^{4+} ions and form Ti^{3+} centers. Through the hydrogenation treatment, H_2 dissociates into H atoms through hydrogen spillover effect on Pt nanoparticles. Later, the hydroxylated
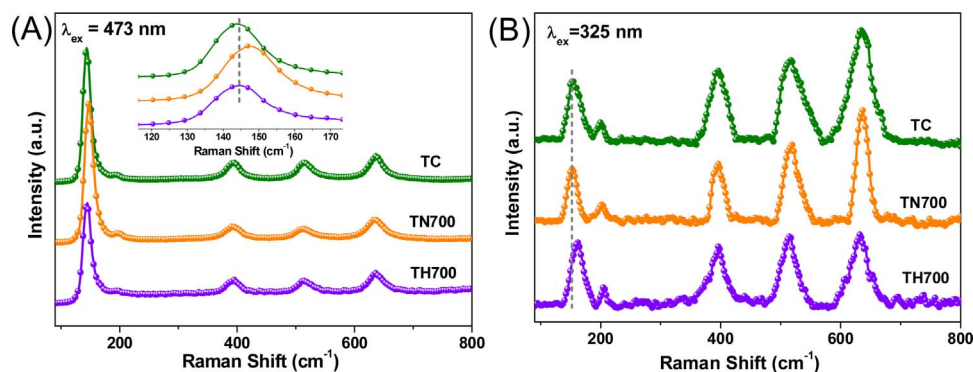

Fig. 9. (A) Visible Raman spectra, and (B) UV Raman spectra of the as-prepared samples. The inset in (A) shows the partial enlarged figure of the samples.
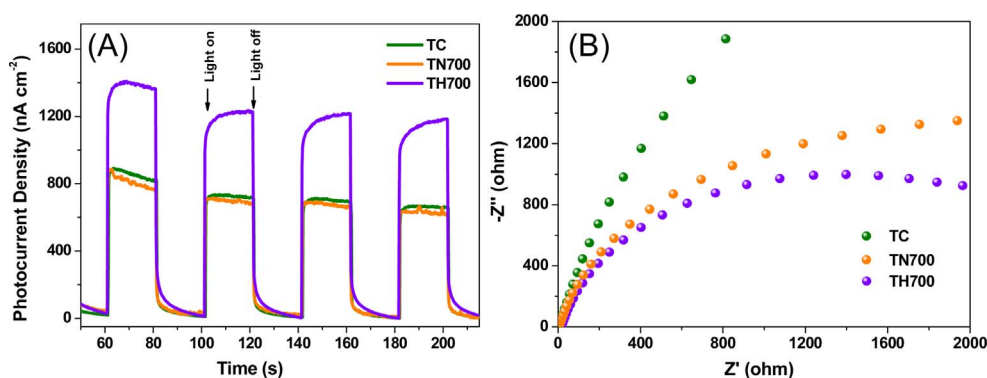
surface is interrupted by H atoms, forming H_2O and surface defects of Ti^{3+} species and V_o's. During the thermal treatment in nitrogen, bulk oxygen atoms migrate to the surface and release in the form of O_2, leaving Ti^{3+} species and V_o's located in bulk region.

Fig. 10A shows the transient chronoamperometry of the samples collected at 0.5 V. All of the samples display prompt and constant on-off responses. The photocurrent density of TH700 is 1.8 and 2.0 times higher than that of the samples of TC and TN700, respectively. Moreover, the EIS results of the samples were collected in Fig. 10B. Compared with the samples of TC and TN700, the sample of TH700 shows the smallest hemicycles in the Nyquist plot, indicating the sample of TH700 is more resistant to charge recombination and has higher charge mobility, which is consistent with the above PL analysis in Fig. 5 [13,53]. Based on above analysis, both surface and bulk defects can increase the separation efficiency of electrons and holes. In addition, compared with bulk defects, the surface defects are more favorable for the improvement of the separation efficiency of photo-generated charge carriers.

Fig. 11A reveals the band gap of the as-prepared samples, which

derived from Tauc equation [54]. The sample of TC exhibits a band gap as high as 3.15 eV. However, the samples of TH700 and TN700 show the decreased band gaps of 3.06 eV and 2.78 eV, respectively. In addition, no notable difference is observed on valence band (VB) XPS among the as-prepared samples, indicating that the samples have the same valence band position (Fig. 11B). Fig. 11C shows the Mott-Schottky plots of the as-prepared samples, the positive slopes can be observed in the Mott-Schottky plots, as expected for *n*-type semiconductors [55]. The smaller slope of the samples of TH700 and TN700 compared with that of the sample of TC, suggesting an increase of donor density. Donor density can be calculated from the slope of Mott-Schottky plots using equation (2) [13,56].

$$N_d = \frac{2/e_0\varepsilon\varepsilon_0}{d(1/C^2)/dV} \tag{2}$$

Where e_0 is the electron charge, ε is the dielectric constant ($\varepsilon = 55$), ε_0 is the permittivity of vacuum, and N_d is the donor density. The calculated electron densities of the samples of TC, TH700 and TN700 are 1.30×10^{14}, 1.15×10^{15} and 3.63×10^{15} cm^{-3}, respectively. The
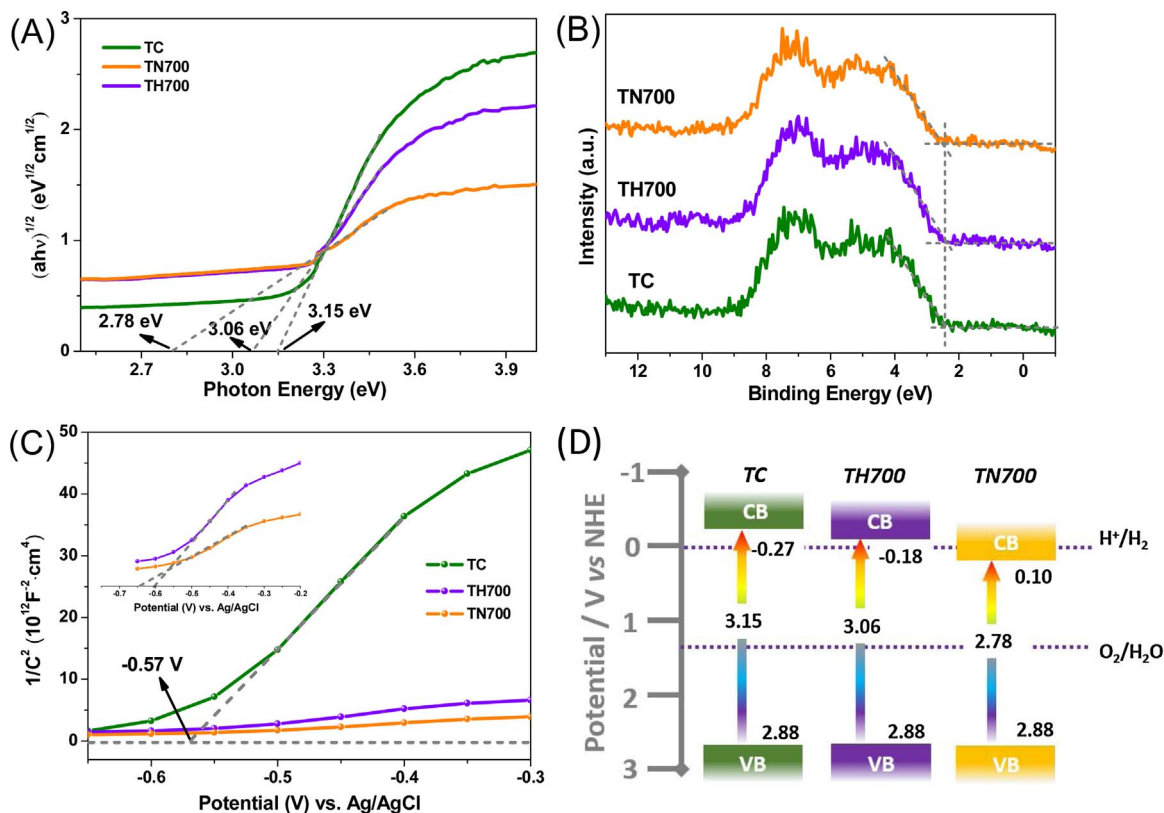

Fig. 11. (A) Tauc plots, (B) Valence band XPS spectra, (C) Mott-Schottky plots, and (D) Energy band diagrams of the samples of TC, TH700, and TN700.

increased donor density of the samples of TN700 and TH700 are owing to the presence of Ti^{3+} species and V_o's in the bulk and surface regions, respectively. And the enhanced donor density can improve the charge transport efficiency in TiO_2. For unmodified semiconductors, flat band position (E_{fb}) is about 0.3 V below the conduction band minimum (CBM) [57]. Thus, CBM of the unmodified sample of TC can be calculated. According to the intercept on the E axis in Mott-Schottky plots, E_{fb} of the sample of TC is determined to be about −0.57 V vs Ag/AgCl. The potential measured according to Ag/AgCl could be converted into normal hydrogen electrode (NHE) potential through equation (3) [57].

$$E_{fb(vs.NHE)} = E_{fb(pH=0,vs.Ag/AgCl)} + E_{AgCl} + 0.059 \times pH \tag{3}$$

Where E_{AgCl} = 0.197 V, the pH value of the electrolyte is 6.8. Thus, the calculated E_{fb} of the sample of TC is 0.03 V vs NHE (pH = 0), and the CBM of the sample of TC is −0.27 V vs NHE. Moreover, valence band maximum (VBM) can be calculated by the equation of VBM = CBM + E_g. Combined with the VB XPS and UV–vis results, the energy band diagram of the samples can be calculated as shown in Fig. 11D. Based on above analysis, the impurity level exists in the band gap of TiO_2 in the form of Ti^{3+}-V_o's states, which determines the conduction band minimum. The surface V_o's and Ti^{3+} centers in the sample of TH700 induce a small tail of conduction band located above the H^+/H_2 redox potential. Thus, it can benefit the photocatalytic activity for hydrogen evolution. Nevertheless, for the sample of TN700 with the Ti^{3+} species and V_o's only located in bulk, the Ti^{3+}-V_o's states extend below the H^+/H_2 redox potential, which inhibits the hydrogen evolution.

The photocatalytic hydrogen evolution over the samples of TH700 and TW-H700 is shown in Fig. S13. The sample of TH700 was prepared by the hydrogenation of TP with surface fluorine, and the sample of TW-H700 was prepared via the hydrogenation of TW without surface fluorine. The two samples exhibit the similar photocatalytic activity for hydrogen production. Since the photocatalytic activity is greatly linked to the generated defects including oxygen vacancies and Ti^{3+} species, we propose that the formation of defects can not be influenced by surface fluorine ions.

Fig. S14 shows the photocatalytic performance of Cr^{6+} reduction of the as-prepared samples. The sample of TH700 with only surface defects exhibits the best performance of Cr^{6+} photoreduction compared with the samples of TC and TN700, which can be ascribed to the enhanced separation efficiency of photo-generated charge carriers, the increased donor density, and the improved light absorption. However, the sample of TN700 with bulk defects shows inhibited activity of Cr^{6+} reduction, which mainly results from the improper band gap structure. A big tail of conduction band is induced by bulk defects, and the downward conduction band minimum inhibits the reduction ability, which is detrimental to the Cr^{6+} photoreduction. The measurements of Cr^{6+} photoreduction can further confirm the changes of properties caused by surface or bulk defects.

4. Conclusions

In summary, we have successfully revealed the relationship between defect distribution (surface and bulk) and photocatalytic activity of hydrogen evolution using TiO_2 with exposed {001} facets as the model catalyst. With the aid of EELS, XPS, XAFS, EPR and UV/Visible Raman, we found that surface Ti^{3+} centers and V_o's generated through the hydrogenation process, and bulk Ti^{3+} species and V_o's could be introduced by the thermal treatment in nitrogen. The induced surface and bulk defects can both increase the light absorption and charge separation efficiency as shown in UV-vis, PL, and EIS results. Compared with bulk defects, the surface defects are more favorable for the improvement of the separation efficiency of photo-generated charge carriers. TiO_2 with bulk defects showed quite low activity for photocatalytic hydrogen evolution compared with the TiO_2 with surface defects. Combined with the VB XPS, UV-vis, and Mott-Schottky plots, we investigated the energy band structures of the as-prepared samples and

revealed that both surface and bulk defects including Ti^{3+} centers and V_o's could induce a defect state which overlapped with conduction band and formed a band tail. After hydrogenation, a small tail of conduction band located above the H^+/H_2 redox potential is generated and thus improves photocatalytic hydrogen evolution. However, the Ti^{3+}-V_o's defect states extend below the H^+/H_2 redox potential for TiO_2 thermally treated in nitrogen, which is detrimental to hydrogen production. The results were further confirmed by the measurements of Cr^{6+} photoreduction. We believe that the favorable energy band structure of hydrogenated TiO_2 with surface Ti^{3+} centers and V_o's is a significant factor to induce the enhanced photocatalytic activity for hydrogen production. In perspective, the rational catalyst design and fabrication strategies in this work are expected to provide guidance for the controllable synthesis of defect-engineered materials for the related catalytic processes.

References

[1] A. Kudo, Y. Miseki, Heterogeneous photocatalyst materials for water splitting, Chem. Soc. Rev. 38 (2009) 253–278.

[2] X. Chen, S.S. Mao, Titanium dioxide nanomaterials: synthesis, properties, modifications, and applications, Chem. Rev. 107 (2007) 2891–2959.

[3] X. Chen, S. Shen, L. Guo, S.S. Mao, Semiconductor-based photocatalytic hydrogen generation, Chem. Rev. 110 (2010) 6503–6570.

[4] Z. Zhao, H. Tan, H. Zhao, Y. Lv, L.J. Zhou, Y. Song, Z. Sun, Reduced TiO_2 rutile nanorods with well-defined facets and their visible-light photocatalytic activity, Chem. Commun. 50 (2014) 2755–2757.

[5] M.M. Khan, S.A. Ansari, D. Pradhan, M.O. Ansari, D.H. Han, J. Lee, M.H. Cho, Band gap engineered TiO_2 nanoparticles for visible light induced photoelectrochemical and photocatalytic studies, J. Mater. Chem. A 2 (2014) 637–644.

[6] L. Liu, Y. Jiang, H. Zhao, J. Chen, J. Cheng, K. Yang, Y. Li, Engineering coexposed {001} and {101} facets in oxygen-deficient TiO_2 nanocrystals for enhanced CO_2 photoreduction under visible light, ACS Catal. 6 (2016) 1097–1108.

[7] W.J. Ong, L.L. Tan, S.P. Chai, S.T. Yong, A.R. Mohamed, Highly reactive {001} facets of TiO_2-based composites: synthesis, formation mechanism and characterization, Nanoscale 6 (2014) 1946–2008.

[8] W. Zhou, W. Li, J.Q. Wang, Y. Qu, Y. Yang, Y. Xie, K. Zhang, L. Wang, H. Fu, D. Zhao, Ordered mesoporous black TiO_2 as highly efficient hydrogen evolution photocatalyst, J. Am. Chem. Soc. 136 (2014) 9280–9283.

[9] J.H. Pan, G. Han, R. Zhou, X.S. Zhao, Hierarchical N-doped TiO_2 hollow microspheres consisting of nanothorns with exposed anatase {101} facets, Chem. Commun. 47 (2011) 6942–6944.

[10] X. Chen, L. Liu, P.Y. Yu, S.S. Mao, Increasing solar absorption for photocatalysis with black hydrogenated titanium dioxide nanocrystals, Science 331 (2011) 746–750.

[11] Y. Zhu, D. Liu, M. Meng, H_2 spillover enhanced hydrogenation capability of TiO_2 used for photocatalytic splitting of water: a traditional phenomenon for new applications, Chem. Commun. 50 (2014) 6049–6051.

[12] J.H. Yang, D.G. Wang, H.X. Han, C. Li, Roles of cocatalysts in photocatalysis and photoelectrocatalysis, Acc. Chem. Res. 46 (2013) 1900–1909.

[13] K.F. Zhang, W. Zhou, L.N. Chi, X.C. Zhang, W.Y. Hu, B.J. Jiang, K. Pan, G.H. Tian, Z. Jiang, Black N/H-TiO_2 nanoplates with a flower-like hierarchical architecture for photocatalytic hydrogen evolution, ChemSusChem 9 (2016) 2841–2848.

[14] Y. Liu, C. Xiao, Z. Li, Y. Xie, Vacancy engineering for tuning electron and phonon structures of two-dimensional materials, Adv. Energy Mater. 6 (2016) 1600436.

[15] M. Kong, Y. Li, X. Chen, T. Tian, P. Fang, F. Zheng, X. Zhao, Tuning the relative concentration ratio of bulk defects to surface defects in TiO_2 nanocrystals leads to high photocatalytic efficiency, J. Am. Chem. Soc. 133 (2011) 16414–16417.

[16] J. Yan, G. Wu, N. Guan, L. Li, Z. Li, X. Cao, Understanding the effect of surface/bulk defects on the photocatalytic activity of TiO_2: anatase versus rutile, Phys. Chem. Chem. Phys. 15 (2013) 10978–10988.

[17] T. Leshuk, R. Parviz, P. Everett, H. Krishnakumar, R.A. Varin, F. Gu, Photocatalytic activity of hydrogenated TiO_2, ACS Appl. Mater. Interfaces 5 (2013) 1892–1895.

[18] X. Liu, G. Zhu, X. Wang, X. Yuan, T. Lin, F. Huang, Progress in black titania: a new

material for advanced photocatalysis, Adv. Energy Mater. 6 (2016) 1600452.

[19] Z. Pei, S. Weng, P. Liu, Enhanced photocatalytic activity by bulk trapping and spatial separation of charge carriers: a case study of defect and facet mediated TiO₂, Appl. Catal., B 180 (2016) 463–470.

[20] H.G. Yang, C.H. Sun, S.Z. Qiao, J. Zou, G. Liu, S.C. Smith, H.M. Cheng, G.Q. Lu, Anatase TiO₂ single crystals with a large percentage of reactive facets, Nature 453 (2008) 638–642.

[21] J.G. Yu, J.X. Low, W. Xiao, P. Zhou, M. Jaroniec, Enhanced photocatalytic CO₂-reduction activity of anatase TiO₂ by coexposed {001} and {101} facets, J. Am. Chem. Soc. 136 (2014) 8839–8842.

[22] J. Pan, G. Liu, G.Q. Lu, H.M. Cheng, On the true photoreactivity order of {001} {010}, and {101} facets of anatase TiO₂ crystals, Angew. Chem. Int. Ed. 50 (2011) 2133–2137.

[23] W. Wang, Y. Ni, C. Lu, Z. Xu, Hydrogenation of TiO₂ nanosheets with exposed {001} facets for enhanced photocatalytic activity, RSC Adv. 2 (2012) 8286–8288.

[24] X. Yu, B. Kim, Y.K. Kim, Highly enhanced photoactivity of anatase TiO₂ nano-crystals by controlled hydrogenation-induced surface defects, ACS Catal. 3 (2013) 2479–2486.

[25] S. Chen, D. Li, Y. Liu, W. Huang, Morphology-dependent defect structures and photocatalytic performance of hydrogenated anatase TiO₂ nanocrystals, J.Catal 341 (2016) 126–135.

[26] X. Chen, L. Liu, F. Huang, Black titanium dioxide (TiO₂) nanomaterials, Chem. Soc. Rev. 44 (2015) 1861–1885.

[27] Y. Wang, J. Cai, M. Wu, H. Zhang, M. Meng, Y. Tian, T. Ding, J. Gong, Z. Jiang, X. Li, Hydrogenated cagelike titania hollow spherical photocatalysts for hydrogen evolution under simulated solar light irradiation, ACS Appl. Mater. Interfaces 8 (2016) 23006–23014.

[28] Z. Wang, C. Yang, T. Lin, H. Yin, P. Chen, D. Wan, F. Xu, F. Huang, J. Lin, X. Xie, M. Jiang, H-doped black titania with very high solar absorption and excellent photocatalysis enhanced by localized surface plasmon resonance, Adv. Funct. Mater. 23 (2013) 5444–5450.

[29] J. Cai, Y. Zhu, D. Liu, M. Meng, Z. Hu, Z. Jiang, Synergistic effect of titanate-anatase heterostructure and hydrogenation-induced surface disorder on photocatalytic water splitting, ACS Catal. 5 (2015) 1708–1716.

[30] J. Cai, Y. Wang, Y. Zhu, M. Wu, H. Zhang, X. Li, Z. Jiang, M. Meng, In situ formation of disorder-engineered TiO₂(B)-anatase heterophase junction for enhanced photocatalytic hydrogen evolution, ACS Appl. Mater. Interfaces 7 (2015) 24987–24992.

[31] T. Lin, C. Yang, Z. Wang, H. Yin, X. Lu, F. Huang, J. Lin, X. Xie, M. Jiang, Effective nonmetal incorporation in black titania with enhanced solar energy utilization, Energy Environ. Sci. 7 (2014) 967–972.

[32] Z. Wang, C. Yang, T. Lin, H. Yin, P. Chen, D. Wan, F. Xu, F. Huang, J. Lin, X. Xie, M. Jiang, Visible-light photocatalytic, solar thermal and photoelectrochemical properties of aluminium-reduced black titania, Energy Environ. Sci. 6 (2013) 3007–3014.

[33] Y. Yan, B. Hao, D. Wang, G. Chen, E. Markweg, A. Albrecht, P. Schaaf, Understanding the fast lithium storage performance of hydrogenated TiO₂ nano-particles, J. Mater. Chem. A 1 (2013) 14507–14513.

[34] F. Tian, Y.P. Zhang, J. Zhang, C.X. Pan, Raman spectroscopy: a new approach to measure the percentage of anatase TiO₂ exposed (001) facets, J. Phys. Chem. C 116 (2012) 7515–7519.

[35] J.W. Xue, X.D. Zhu, Y. Zhang, W.D. Wang, W. Xie, J.L. Zhou, J. Bao, Y. Luo, X. Gao, Y. Wang, L.Y. Jang, S. Sun, C. Gao, Nature of conduction band tailing in hydro-genated titanium dioxide for photocatalytic hydrogen evolution, ChemCatChem 8 (2016) 2010–2014.

[36] Y.Z. Li, D.S. Hwang, N.H. Lee, S.J. Kim, Synthesis and characterization of carbon-doped titania as an artificial solar light sensitive photocatalyst, Chem. Phys. Lett. 404 (2005) 25–29.

[37] M. D'Arienzo, M.V. Dozzi, M. Redaelli, B.D. Credico, F. Morazzoni, R. Scotti, S. Polizzi, Crystal surfaces and fate of photogenerated defects in shape-controlled anatase nanocrystals: drawing useful relations to improve the H₂ yield in methanol photosteam reforming, J. Phys. Chem. C 119 (2015) 12385–12393.

[38] M. D'Arienzo, J. Carbajo, A. Bahamonde, M. Crippa, S. Polizzi, R. Scotti, L. Wahba,

[39] F. Morazzoni, Photogenerated defects in shape-controlled TiO₂ anatase nanocrys-tals: a probe to evaluate the role of crystal facets in photocatalytic processes, J. Am. Chem. Soc. 133 (2011) 17652–17661.

[39] H. Cheng, A. Selloni, Surface and subsurface oxygen vacancies in anatase TiO₂ and differences with rutile, Phys. Rev. B 79 (2009) 092101.

[40] C. Di Valentin, G. Pacchioni, A. Selloni, Electronic structure of defect states in hydroxylated and reduced rutile TiO₂(110) surfaces, Phys. Rev. Lett. 97 (2006) 166803.

[41] Y. Yan, M. Han, A. Konkin, T. Koppe, D. Wang, T. Andreu, G. Chen, U. Vetter, J. Ramon Morante, P. Schaaf, Slightly hydrogenated TiO₂ with enhanced photo-catalytic performance, J. Mater. Chem. A 2 (2014) 12708–12716.

[42] A. Naldoni, C.L. Bianchi, C. Pirola, K.S. Suslick, Porous TiO₂ microspheres with tunable properties for photocatalytic air purification, Ultrason. Sonochem. 20 (2013) 445–451.

[43] S. Ardizzone, C.L. Bianchi, G. Cappelletti, S. Gialanella, C. Pirola, V. Ragaini, Tailored anatase/brookite nanocrystalline TiO₂. the optimal particle features for liquid and gas phase photocatalytic reactions, J. Phys. Chem. C 111 (2007) 13222–13231.

[44] J. Li, C.H. Liu, X. Li, Z.Q. Wang, Y.C. Shao, S.D. Wang, X.L. Sun, W.F. Pong, J.H. Guo, T.K. Sham, Unraveling the origin of visible light capture by core-shell TiO₂ nanotubes, Chem. Mater. 28 (2016) 4467–4475.

[45] T.K. Das, P. Ilaiyaraja, P.S.V. Mocherla, G.M. Bhalerao, C. Sudakar, Influence of surface disorder, oxygen defects and bandgap in TiO₂ nanostructures on the pho-tovoltaic properties of dye sensitized solar cells, Sol. Energy Mater. Sol. Cells 144 (2016) 194–209.

[46] A. Naldoni, M. Allieta, S. Santangelo, M. Marelli, F. Fabbri, S. Cappelli, C.L. Bianchi, R. Psaro, V. Dal Santo, Effect of nature and location of defects on bandgap nar-rowing in black TiO₂ nanoparticles, J. Am. Chem. Soc. 134 (2012) 7600–7603.

[47] Y.F. Xu, C. Zhang, L.X. Zhang, X.H. Zhang, H.L. Yao, J.L. Shi, Pd-catalyzed instant hydrogenation of TiO₂ with enhanced photocatalytic performance, Energy Environ. Sci. 9 (2016) 2410–2417.

[48] M. Salari, K. Konstantinov, H.K. Liu, Enhancement of the capacitance in TiO₂ na-notubes through controlled introduction of oxygen vacancies, J. Mater. Chem. 21 (2011) 5128–5133.

[49] J. Zhang, M.J. Li, Z.C. Feng, J. Chen, C. Li, UV Raman spectroscopic study on TiO₂. I. phase transformation at the surface and in the bulk, J. Phys. Chem. B 110 (2006) 927–935.

[50] C. Li, M.J. Li, UV Raman spectroscopic study on the phase transformation of ZrO₂, Y₂O₃-ZrO₂ and SO₄²⁻/ZrO₂, J. Raman Spectrosc. 33 (2002) 301–308.

[51] M. Guo, J.Q. Lu, Y.N. Wu, Y.J. Wang, M.F. Luo, UV and visible Raman studies of oxygen vacancies in rare-earth-doped ceria, Langmuir 27 (2011) 3872–3877.

[52] K. Lv, Q. Xiang, J. Yu, Effect of calcination temperature on morphology and pho-tocatalytic activity of anatase TiO₂ nanosheets with exposed {001} facets, Appl. Catal., B 104 (2011) 275–281.

[53] J. Cai, M. Wu, Y. Wang, H. Zhang, M. Meng, Y. Tian, X. Li, J. Zhang, L. Zheng, J. Gong, Synergetic enhancement of light harvesting and charge separation over surface-disorder-engineered TiO₂ photonic crystals, Chem 2 (2017) 877–892.

[54] J. Ng, S. Xu, X. Zhang, H.Y. Yang, D.D. Sun, Hybridized nanowires and cubes: a novel architecture of a heterojunctioned TiO₂/SrTiO₃ thin film for efficient water splitting, Adv. Funct. Mater. 20 (2010) 4287–4294.

[55] G. Wang, H. Wang, Y. Ling, Y. Tang, X. Yang, R.C. Fitzmorris, C. Wang, J.Z. Zhang, Y. Li, Hydrogen-treated TiO₂ nanowire arrays for photoelectrochemical water splitting, Nano Lett. 11 (2011) 3026–3033.

[56] W.Y. Hu, W. Zhou, K.F. Zhang, X.C. Zhang, L. Wang, B.J. Jiang, G.H. Tian, D.Y. Zhao, H.G. Fu, Facile strategy for controllable synthesis of stable mesoporous black TiO₂ hollow spheres with efficient solar-driven photocatalytic hydrogen evolution, J. Mater. Chem. A 4 (2016) 7495–7502.

[57] W.J. Yin, L.J. Bai, Y.Z. Zhu, S.X. Zhong, L.H. Zhao, Z.Q. Li, S. Bai, Embedding metal in the interface of a p-n heterojunction with a stack design for superior Z-scheme photocatalytic hydrogen evolution, ACS Appl. Mater. Interfaces 8 (2016) 23133–23142.